An Experimental Investigation on the Characteristics of Turbulent Boundary Layer Flows Over a Dimpled Surface

Wenwu Zhou
Department of Aerospace Engineering,
Iowa State University,
Ames, IA 50011

Yu Rao
Gas Turbine Research Institute,
School of Mechanical Engineering,
Shanghai Jiao Tong University,
Shanghai 200240, China
e-mail: yurao@sjtu.edu.cn

Hui Hu[1]
Department of Aerospace Engineering,
Iowa State University,
Ames, IA 50011
e-mail: huhui@iastate.edu

An experimental investigation was conducted to quantify the characteristics of the turbulent boundary layer flows over a dimpled surface in comparison to those over a conventional flat plate. In addition to measuring surface pressure distributions to determine the friction factors of the test plates and to map the surface pressure inside the dimple cavity, a high-resolution digital particle image velocimetry (PIV) system was used to achieve detailed flow field measurements to quantify the characteristics of the turbulent boundary layer flows over the test plates and the evolution of the unsteady vortex structures inside the dimple cavity at the middle of the dimpled test plate. It was found that the friction factor of the dimpled plate would be about 30–80% higher than that of the flat plate, depending on the Reynolds number of the test cases. In comparison with those over a conventional flat surface, the flow characteristics of the turbulent boundary layer flows over the dimpled surface were found to be much more complicated with much stronger near-wall Reynolds stress and higher turbulence kinetic energy (TKE) levels, especially in the region near the back rims of the dimples. Many interesting flow features over the dimple surface, such as the separation of oncoming boundary layer flow from the dimpled surface when passing over the dimple front rim, the formation and periodic shedding of unsteady Kelvin–Helmholtz vortices in the shear layer over the dimple, the impingement of the high-speed incoming flow onto the back rim of the dimple, and the subsequent generation of strong upwash flow in the boundary flow to promote the turbulent mixing over the dimpled surface, were revealed clearly and quantitatively from the PIV measurement results. The quantitative measurement results are believed to be the first of its nature, which depict a vivid picture about the unique flow features over dimpled surfaces and their correlations with the enhanced heat transfer performance reported in previous studies. [DOI: 10.1115/1.4031260]

1 Introduction

Modern gas turbines operate at a peak turbine inlet temperature well beyond the maximum endurable temperature of the turbine blade material. As a result, hot gas-contacting turbine blades have to be cooled intensively by using various cooling techniques, such as internal convective cooling [1–20] and film cooling [21–24] on the blade exterior, in order to ensure a good structural integrity of the turbine blades. Dimple arrays, which can be placed throughout the entire internal cooling passage of turbine blades incorporating with other augmentation methods (such as impingement holes, rib turbulator, and pin-fins), have become a magnet in forced convective heat transfer studies in recent years [1–19]. Due to its good heat transfer enhancement performance with comparatively smaller pressure loss penalties in comparison to other types of heat transfer augmentation devices such as pin-fins and rib tabulators, a dimpled surface (i.e., a flat surface with dimple arrays) provides a desirable alternative for the internal cooling of turbine blades, especially in the rear regions of turbine blades.

A number of experimental and numerical studies have been conducted in recent years to investigate heat transfer augmentation performance of dimpled surfaces [3–7,9–13,15–19]. It is found that the heat transfer performance of a dimpled surface is greatly affected by the configuration of the dimples, including dimple diameter, dimple depth ratio, distribution pattern, and shape of the dimples. Terekhov et al. [12] conducted an experimental study to measure the heat transfer coefficient and aerodynamic resistance of a dimpled surface, and found that the augmentation of heat transfer is much greater than that of flow resistance, leading to an overall increase in the rate of heat transfer process. Mahmood et al. [7] and Ligrani et al. [3,19] studied the local heat transfer and flow structures over dimpled surfaces experimentally with Reynolds numbers (based on channel height H) changing from 1250 to 61,500, dimple depth ratio of 0.2, and channel height to dimple diameter ratio of 0.5. Based on qualitative flow visualization with smoke wires, Ligrani et al. [3,19] suggested that unsteady vortex structures shedding from dimples (including upwash flows and packets of vortices generated from the dimples) would enhance the turbulent mixing between the mainstream coolant flow and the hot flow inside the dimple cavity, therefore, leading to an augmentation of local Nusselt numbers over dimpled surfaces. Mahmood and Ligrani [15] conducted an experimental study to investigate the combined influences of channel height ratios (0.2, 0.25, 0.5, and 1.0), temperature ratios (0.78–0.94), Reynolds number (600–11,000), and flow structures on the heat transfer process over dimpled surfaces. They found that, as the channel height H/D decreases, both the shedding of unsteady vortex structures and local Nusselt numbers become greater. Mitsudharmadi et al. [5] investigated the effects of round edged dimple arrays on the development of boundary layer flows over dimpled surfaces with depth ratios of 4%, 8%, and 12%. Their measurements revealed that the flow separation observed for the test case with deeper edged dimples has similar flow structures as those of the cases with sharp dimple edge. Jordan et al. [6] conducted detailed measurements of Nusselt number

[1]Corresponding author.

Contributed by the Fluids Engineering Division of ASME for publication in the Journal of Fluids Engineering. Manuscript received March 15, 2015; final manuscript received July 29, 2015; published online September 10, 2015. Assoc. Editor: Mark F. Tachie.

distributions over an array of V-shaped dimples using both transient liquid crystal and temperature sensitive pain technique. Their measurements results indicate that V-shaped dimples appear to enhance heat transfer augmentation with Reynolds number increasing, while marginal increase of pressure drop. As reported in Bunker et al. [17], dimple arrays were found to enhance heat transfer process not only in rectangular channels, but also in circular tubes was well. Based on the numerical simulation results with a large eddy simulation (LES) method, Turnow et al. [16] claimed that the fluctuations of streamwise velocity and the turbulent vortex structures are responsible for the augmentation of heat transfer over a dimpled surface. More recently, Xie et al. [4] conducted a numerical study to compare the surface heat transfer enhancement of six different shaped dimples, and found that the greatest heat transfer enhancement would be reached when the largest cross section area of the dimple is oriented to be perpendicular to the incoming flow direction. Rao et al. [9] conducted an experimental and numerical study on teardrop shaped dimples and reported that teardrop shaped dimples exhibit the highest heat transfer ratio among all the tested shapes, which is about 18% higher than conventional spherical dimples.

While many significant findings have already been uncovered through those previous studies, most of the previous studies focused mainly on global features of the enhanced heat transfer over dimpled surfaces, very few studies can be found in literature to provide detailed flow field measurements to quantify the unique characteristics of the boundary layer flows over dimpled surfaces and/or inside dimple cavities. While the unsteady vortex structures generated inside dimple cavities were suggested to play a very important role for the heat transfer augmentation over dimpled surfaces [3,7,19], most of the previous studies were conducted by using smoke wires to qualitatively visualize the unsteady vortex structures over dimpled surfaces or/and inside dimple cavities, no quantitative measurements have ever been available to characterize the evolution of the unsteady vortex structures over dimpled surfaces and/or inside dimple cavities. Such quantitative information is highly desirable to elucidate underlying physics for improved heat transfer performance of dimpled surfaces.

In the present study, an experimental investigation was conducted to quantify the characteristics of the turbulent boundary layer flows over a dimpled surface with staggered dimple arrays, in comparison to those over a conventional flat plate. The experimental study was conducted in a low-speed, open-circuit wind tunnel with the Reynolds number (i.e., based on the hydraulic diameter of the dimpled channel and freestream velocity) in the range of $Re = 8200–50{,}500$, i.e., in the range of the Reynolds numbers for internal cooling channel of gas turbine blades. In addition to measuring surface pressure distributions to determine the friction factors of the test plates, a high-resolution digital PIV system was utilized to achieve detailed flow field measurements to quantify the characteristics of turbulent boundary layer flows over the test plates and to reveal the evolution of the unsteady vortex structures inside the dimple cavity. The detailed flow field measurements were correlated with the surface pressure measurement data to gain further insight into underlying physics to explore/optimize design paradigms for better internal cooling designs to protect turbine blades from the extremely harsh environments.

2 Test Models and Experimental Setup

2.1 Test Models. The experimental study was performed in a low-speed, open-circuit wind tunnel located at the Department of Aerospace Engineering of Iowa State University. Similar as those used in previous studies [1–5], a rectangular channel with a small aspect ratio was designed to simulate the channel flow inside the internal cooling channel of gas turbine blades. The tunnel has an optically transparent test section of $20\,mm \times 152\,mm$ in cross section ($H/W = 0.132$) with a corresponding hydraulic diameter (D_h) of 35.4 mm (i.e., $D_h = 35.4$ mm). The airflow in the wind tunnel is driven by a centrifugal blower. A settling chamber with honeycomb, screen structures and a contraction section with an area ratio of 10:1 are installed at the upstream of the test section in order to provide uniform low turbulent incoming flow into the test section. The turbulence intensity level of the airflow in the test section of the wind tunnel was found to be about 1.0%, as measured by hotwire anemometer. In the present study, 2-in.-wide 64 grit sand papers were employed on both the top and bottom surfaces of the inlet duct (i.e., 14 D_h distance upstream of the test plate) in order to trip the oncoming boundary layer flow at the entrance of the test plate to ensure a fully developed turbulent boundary layer flow over the test plate.

Figure 1 shows the schematic of a dimpled test plate along with a conventional flat plate as the comparison baseline used in the present study. As shown in Fig. 1, the two test plates are designed to have the same dimension, i.e., 275 mm in length, 170 mm in width and 12.7 mm in thickness. The test plates are made of hard plastic and manufactured by using a rapid prototyping machine. For the dimpled test plate, an array of spherical dimples with the same diameter of 20 mm and sharp edges (i.e., $D = 20$ mm and spherical diameter of 29 mm) are distributed uniformly on the test plate in a staggered pattern. The distances between the adjacent dimples in both streamwise and spanwise directions are the same, i.e., $P = 25$ mm. The depth of the dimples is set to be $h = 4$ mm with the corresponding depth ratio of $h/D = 0.2$. It should be noted that the depth of the dimple is relatively large to the channel height, 20 mm. Considering fluid with 25% of local cross-sectional change in the main flow direction, the flow inside dimple cavity could be regarded as pulsatile internal flow along the main stream, rather than the effect on single-surface boundary layer. During the experiments, the dimpled test plate was flush mounted onto the bottom plate of the test section to form a narrow test channel. The arrangement of dimple arrays over the dimpled test plate used in the present study is very similar as that used in Mahmood and Ligrani [15].

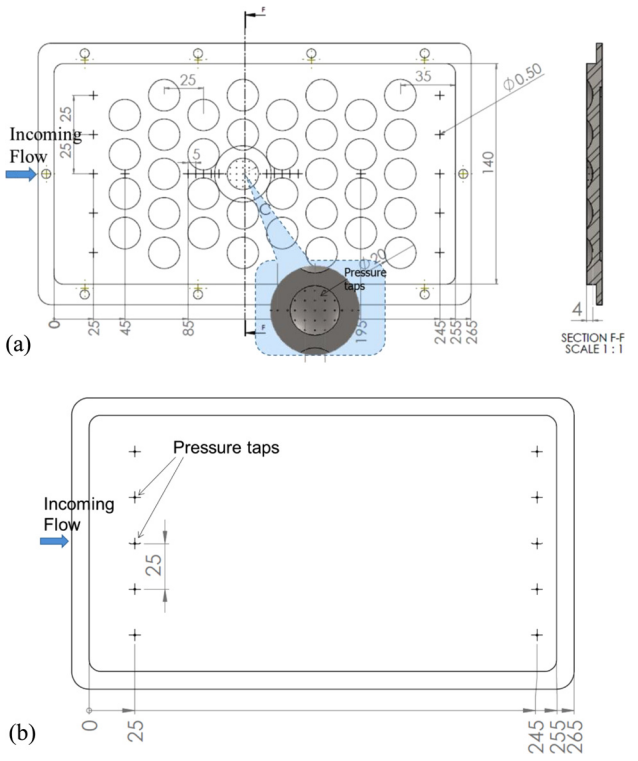

Fig. 1 Schematic of the two test plates used in the present study (unit in mm): (*a*) a dimpled test plate and (*b*) a conventional flat test plate

A total amount of 45 pressure taps with 0.5 mm in diameter for each taps were arranged over the dimpled test plate in order to map the surface pressure distributions on the test plate. While 21 pressure taps were distributed uniformly inside the dimple at the center of the test plate, five pressure taps in each group were located at the leading and trailing edges of test plate, and the rest of the 14 pressure taps were arranged along the centerline of test plate. The pressure taps were connected to three units of digital sensor arrays (DSA3217, Scanivalve Corp., Liberty Lake, WA 16 channels for each unit) by using tygon tubing with 1.5 mm diameter and 0.5 m length for the pressure data acquisition. The DSA3217 system incorporates temperature-compensated piezoresistive pressure sensors with a pneumatic calibration valve, RAM, 16 bit A/D converter, and a microprocessor in a compact self-contained module. The precision of the pressure acquisition system is ±0.05% of the ±10 in. H_2O full scale range. During the experiments, the instantaneous surface pressure measurement data for each pressure tap were acquired at a data acquisition rate of 300 Hz for 100 s.

It should be noted that, since Reynolds number based on either channel height or hydraulic diameter of the rectangular test channel has been widely used in the previous studies to investigate the flow characteristics and heat transfer performance of internal cooling designs of gas turbine blades, same definition of Reynolds number is also used in the present study in order to correlate the measurement results of the present study to those of the previous studies [1–8]. During the experiments, the central line flow velocity of the rectangular test section was set to change from $\bar{U}$ = 4–22 m/s, and the corresponding Reynolds number based on the hydraulic diameter (D_h) of the rectangular channel varies from Re = 8200–50,500, which is in the range of the typical Reynolds numbers of the channel flows to study internal cooling of gas turbine blades [9,15]. The Reynolds number levels of the test cases based on the dimple diameter (D) and the channel height (H) are also listed in Table 1 for comparison.

2.2 Experimental Setup for PIV Measurements. Figure 2 shows the schematic of the experimental setup used for PIV measurements. The incoming airflow was seeded with ~1 μm oil droplets generated by a fog seeding machine. Illumination was provided by a double-pulsed Nd:YAG laser (NewWave Gemini PIV 200) adjusted on the second harmonic and emitting two laser pulses of 200 mJ at the wavelength of 532 nm with a repetition rate of 5 Hz. The laser beam was shaped to a thin sheet by a set of mirrors, spherical, and cylindrical lenses. The thickness of the laser sheet in the measurement region was set to be about 0.8 mm. During the experiments, the illuminating laser sheet was first aligned vertically along the incoming flow direction (i.e., in the X–Y plane as shown in Fig. 2) passing the symmetric plane of the dimpled test plate, which were used to determine the ensemble-averaged velocity field, Reynolds stress and in-plane TKE distributions of the boundary layer flow over the dimpled surface in the X–Y plane. Then, the illuminating laser sheet was rotated 90 deg for the PIV measurements in the X–Z plane at about 1.5 mm above the dimpled test plate. A high-resolution 14-bit (2048 pixels × 2048 pixels) charge-coupled device (CCD) camera (PCO2000, Cooke Corp.; PCO-TECH, Romulus, MI) with its view axis normal to the illuminating laser sheet (i.e., for both of the test cases with the laser sheet in X–Y plane and X–Z plane) was used for PIV image recording, which has a field of view 45 × 25 mm^2 and a magnification of 0.025 mm/pix.

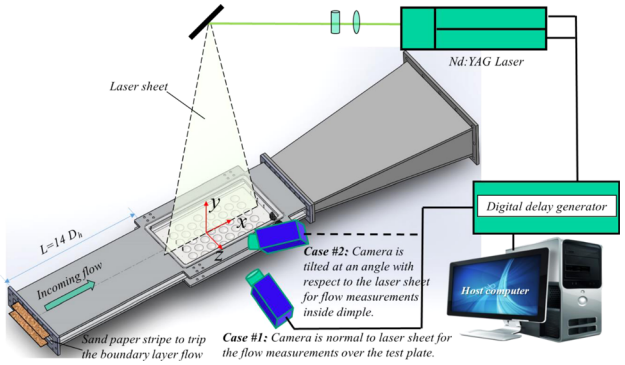

Fig. 2 Experimental setup for PIV measurements

The CCD camera and the double-pulsed Nd:YAG lasers were connected to a workstation (host computer) via a Digital Delay Generator (Berkeley Nucleonics, Model 565, San Rafael, CA), which controlled the time interval of the laser illumination and the image acquisition.

In the present study, PIV measurements were also conducted with the CCD camera tilted at an angle of ~30 deg with respect to the vertically aligned illuminating laser sheet (i.e., X–Y plane) passing the symmetric plane of the dimpled test plate, as shown in Fig. 2, in order to quantify the turbulent flow and unsteady vortex structures inside the dimple cavity. A tilt-axis mount was installed between the lens and the camera body to satisfy the Scheimpflug condition to ensure that the tracer particles in the laser sheet (i.e., objective plane) being focused on the image planes. Since the image plane of the CCD camera is tilted with respect to the objective plane for such a setting, the magnification factors between the image plane and the object plane are variable due to the perspective distortion. An in situ calibration procedure as suggested by Soloff et al. [25] was conducted in the present study to obtain the quantitative mapping functions between the image plane and the object plane for the PIV measurements to reveal unsteady vortex structures inside the dimple cavity. It should also be noted that, in order to alleviate the contaminations of the strong laser reflection from the surfaces of the test plates to the acquired PIV raw images, the test plates were coated with a layer of Rhodamine 6G dye. Meanwhile, a 532 nm band pass filter was mounted in front of the optical lens of the CCD camera to filter out the laser-induced fluorescence from the Rhodamine 6G coated surfaces. Since the adhesion of tiny oil droplets (i.e., PIV tracers) onto the channel walls during the experiments may affect PIV measurements, the test plate was removed from the test rig for a thorough clean after each test run in order to minimize the effects of the oil droplet deposition on the PIV measurements.

After PIV image acquisition, instantaneous velocity vectors were obtained by frame to frame cross-correlation of particle images, using an interrogation window of 32 pixels × 32 pixels. An effective overlap of 50% of the interrogation windows was employed in PIV image processing, which results in a spatial resolution of 0.4 mm for the PIV measurements. After the instantaneous velocity vectors (u_i v_i) were determined, the distributions of the ensemble-averaged flow quantities such as averaged velocity, normalized Reynolds Shear Stress ($\tilde{\tau} = -\overline{u'v'}/\bar{U}^2$), and normalized in-plane TKE (i.e., $0.5(\overline{u'^2} + \overline{v'^2})/\bar{U}^2$ in X–Y plane or

Table 1 Reynolds numbers of the three test cases

Test cases	Reynolds number based on hydraulic diameter, D_h	Reynolds number based on dimple diameter (D) or height (H)	Reynolds number based momentum thickness (θ)
Case 1	8.2	4.6	306
Case 2	36.7	20.7	1187
Case 3	50.5	28.5	1370

$0.5(\overline{u'^2} + \overline{w'^2})/\bar{U}^2$ in X–Z plane) were obtained from a sequence of about 1000 frames of instantaneous PIV measurements, where $\bar{U}$ is the spatial averaged velocity of cross section (bulk velocity). The measurement uncertainty level for the instantaneous velocity vectors is estimated to be within 3.0%, while the uncertainties for the measurements of the ensemble-averaged flow quantities are estimated to be within 7.0%.

3 Results and Discussion

3.1 Characteristics of the Oncoming Boundary Layer Flow. As described above, sand papers were employed on both the top and bottom surfaces of the inlet duct to trip the boundary layer flows over the top and bottom surfaces. Since the tripped boundary layer flows over both the top and bottom surfaces would develop and eventually merge at the center of test channel, the thickness (δ) of the boundary layer flows would be $0.5H$ (i.e., $\delta = 10$ mm) after becoming fully developed [12,26]. In the present study, the characteristics of the oncoming boundary layer flow at the entrance of the test plate were measured by using the digital PIV system at three different test conditions (Re = 8.2 K, 36.7 K, and 50.5 K). Figure 3 shows the measured velocity profiles of the oncoming boundary layer flow at the entrance of the test plate. It can be seen clearly that, except for the test case of Re = 8.2 K, the velocity profiles of the oncoming boundary layer flow are found to follow a one-seventh power law well, i.e., $U/U_0 = (Y/\delta)^{1/7}$, where U_0 is the velocity at $Y = 0.5H$ height. It indicates a fully developed turbulence boundary layer flow over the test plate. While the momentum thicknesses of the turbulent boundary layer flow was found to be 0.099δ and 0.083δ, the corresponding shape factor (H^*) is 1.31 and 1.32 for the test cases of Re = 36.7 K and Re = 50.5 K, respectively. As for the test case of Re = 8.2 K, the momentum thickness of the boundary layer flow was found to be 0.114δ and shape factor of 1.54.

According to the logarithmic law ($U^+ = (1/\kappa)\ln y^+ + A$, where $\kappa = 0.41$ and $A = 5.2$) of the velocity profiles for a fully developed turbulent channel flow [27], the friction velocity (u_*) and local wall shear stress (τ_w) were also estimated based on the measured flow velocity profiles ($30 \le y^+$, $y \le 0.3\delta$) at the entrance of the test plate, and the results are listed in Table 2.

3.2 Friction Factor Measurement Results. In the present study, the friction factors of the channel flows over the test plates were determined based on the measured surface pressure distributions on the test plates. For a fully developed turbulent channel flow, the friction factor of a test plate can be calculated by using following equation [28–30]:

$$f = \frac{D_h \Delta p}{2L\rho\bar{U}^2} \tag{1}$$

where D_h is the hydraulic diameter of the test section (i.e., $D_h = 35.4$ mm for the present study); Δp is the pressure loss along the dimpled test plate; L is the distance between the two rows of the pressure taps at the inlet and outlet of the dimpled test plate (i.e., $L = 220$ mm); ρ is the density of air flow; $\bar{U}$ is the bulk velocity of the test section. Figure 4 gives the measured friction factors of the dimpled test plate in comparison with those of the flat test plate.

The applicability of Eq. (1) to estimate the friction factor of a fully developed turbulent channel flow was validated by quantitatively comparing the measured friction factors of the flat test plate with those predicted by using an empirical formula suggested by Dean [31] (i.e., $f = 0.073\mathrm{Re}^{-0.25}, \mathrm{Re} = \rho\bar{U}D_h/\mu$). As shown in Fig. 4, it is obvious that the measured friction factor of the flat test plate (solid circular marks) agree very well with those predicted by using the empirical formula suggested by Dean [31] within the entire Reynolds number range of the present study (i.e., $10{,}000 < \mathrm{Re} < 60{,}000$). It confirms the applicability of Eq. (1) to estimate the friction factor of fully developed turbulent channel flow over the flat test plate.

As clearly shown in Fig. 4, as the Reynolds number increases, while the friction factor of the flat test plate would decrease gradually, the friction factor of the dimpled surface (solid square marks)

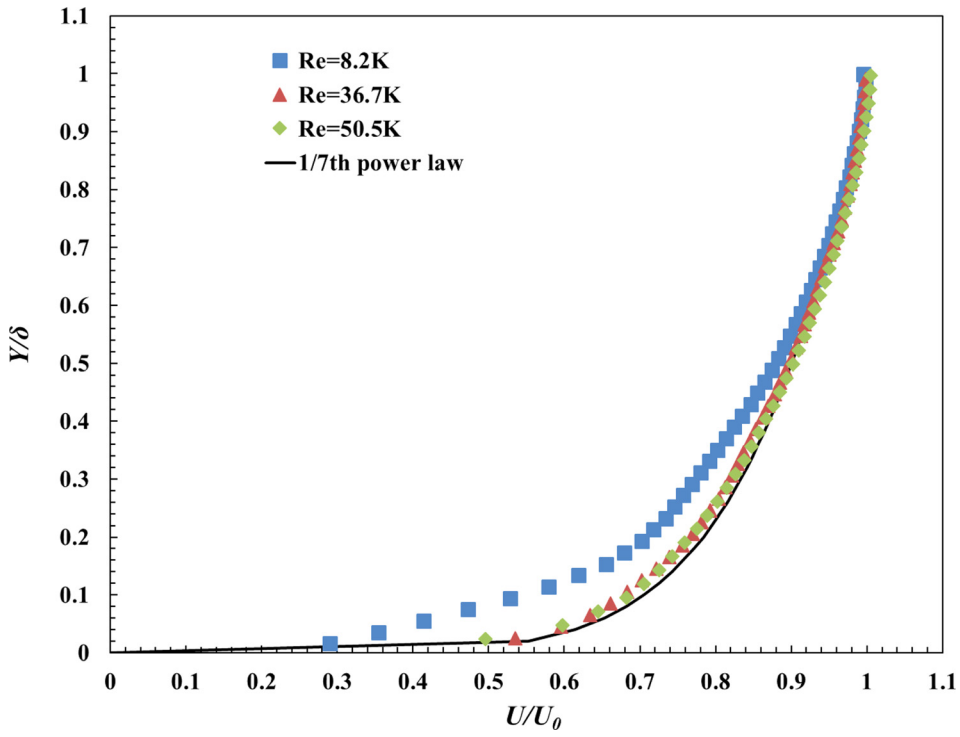

Fig. 3 Measured velocity profiles of the oncoming boundary layer flow at the entrance of test plate for the test cases of Re = 8.2 K, Re = 36.7 K, and Re = 50.5 K, respectively (where U_0 is the maximum flow velocity inside the channel)

Table 2 Flow characteristics of the oncoming boundary layer flow over the test plate

Test cases	Displacement thickness (δ^*)	Momentum thickness (θ)	Shape factor (H^*)	Friction velocity (m/s)	Wall shear stress (N/m^2)
Re = 8.2 K	0.175δ	0.114δ	1.54	—	—
Re = 36.7 K	0.130δ	0.099δ	1.31	0.90	0.96
Re = 50.5 K	0.110δ	0.083δ	1.32	1.14	1.53

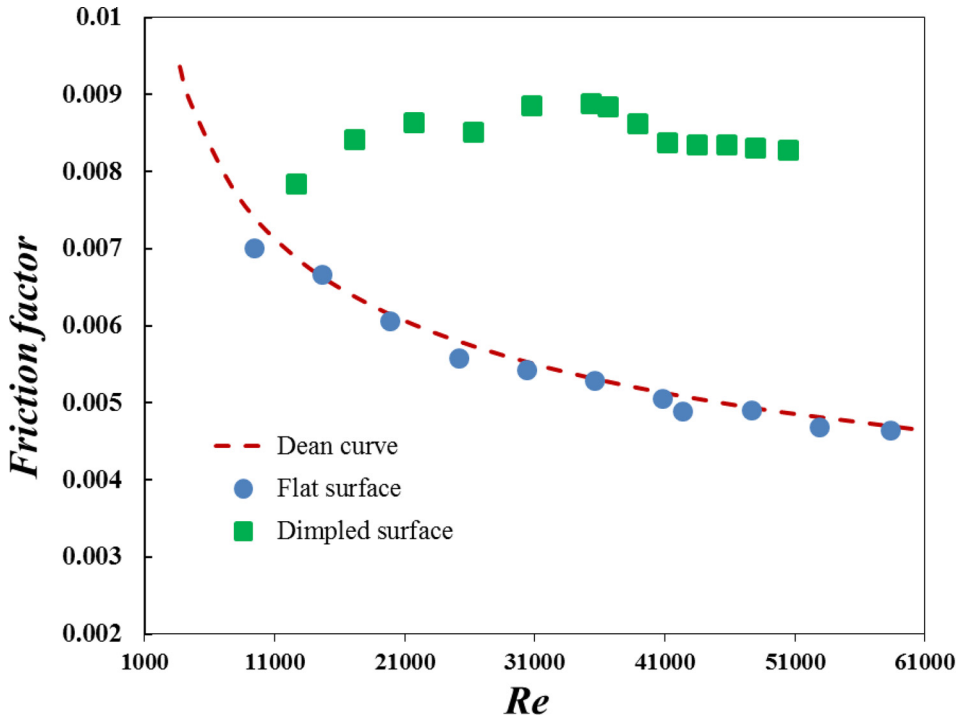

Fig. 4 Measured friction factors of the test plates a function of the Reynolds number

was found to increase rapidly at first, reaching the peak value at Re ≈ 33,000, then decrease slightly with the increasing Reynolds number until Re ≈ 40,000. The friction factor of the dimpled surface was found to become almost constant as the Reynolds number being greater than 41,000 (i.e., Re > 41,000). Compared with those of the flat test plate, the friction factor of the dimpled surface was found to be about 30–80% greater at the same Reynolds number levels. Similar conclusions were also reported in the previous study of Han et al. [2]. The higher friction factor of the dimpled surface as shown in Fig. 4 is believed to be closely related to the more complicated turbulent flow structures induced by the dimple arrays, which will be discussed in Sec. 3.4 of the present study.

3.3 Surface Pressured Distributions Inside the Dimple Cavity. As shown schematically in Fig. 2, 21 pressure taps are arranged inside the dimple at the center of the test plate in order to map the surface pressure coefficient ($C_p = (P - P_1)/\frac{1}{2}\rho\bar{U}^2$) inside the dimple cavity at different test conditions, where P_1 is the static pressure of the incoming flow measured at the inlet of the test section. Figure 5 shows the measured surface pressure coefficient distributions inside the dimple cavity at the test conditions of Re = 8.2 K, 36.7 K, and 50.5 K, respectively.

As shown clearly in Fig. 5, the distribution pattern of the surface pressure coefficients inside the dimple cavity was found to be quite similar in general at different Reynolds number levels. While the surface pressure was found to be relatively low in the region near the front rim of the dimple, a region with much high surface pressure exists near the back rim of the dimple. Such a distribution pattern was found to be closely related to the unique flow characteristics inside the dimple cavity, i.e., the incoming mainstream flow would separate from the dimpled surface when passing over the front rim of the dimple, which leads to the formation of a recirculation region with relatively low surface pressure at the front portion of the dimple cavity. The low pressure at the front portion of the dimple would cause the mainstream flow to shift downward slightly and impinge onto the back rim of the dimple, resulting in a high pressure region near the back rim of the dimple.

While the global features of the surface pressure distribution pattern inside the dimple cavity were found to be quite similar for the three test cases, some differences still can be identified from the comparison of the surface pressure distributions given in Fig. 5. The size of the region with relatively low surface pressure at the front of the dimple cavity was found to become greater as the Reynolds number increases, which is believed to be closely related to the stronger recirculating flow at the front of the dimple cavity for the cases with higher Reynolds numbers.

Figure 6 shows the transverse profiles of the surface pressure coefficients along the centerline of the dimple for the three test cases, which reveals the variations of the surface pressure inside the dimples cavity more clearly and quantitatively. As shown in the plot, the surface pressure inside the dimple cavity was found to decrease slightly at the front of the dimple (i.e., within the recirculation region as revealed from the PIV measurement results to be discussed later), then increase rapidly at the rear portion of the dimple cavity, and reach their peak values at the back rim of the dimple. As described above, while the general trend of the surface pressure profiles at different Reynolds number levels was found to be almost the same, the slightly earlier increase of the surface

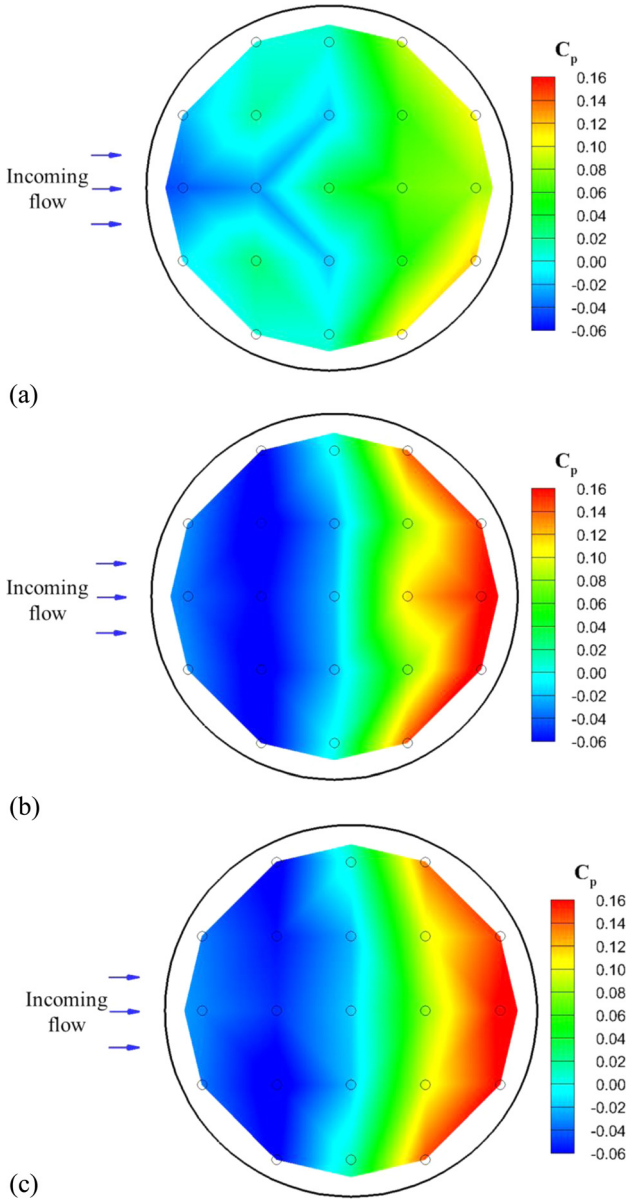

Fig. 5 Measured surface pressure coefficient distributions inside the dimple cavity: (*a*) Re = 8.2 K, (*b*) Re = 36.7 K, and (*c*) Re = 50.5 K

pressure inside the dimple cavity can be observed for the case with the lowest Reynolds number (i.e., Re = 8.2 K case).

3.4 PIV Measurements to Quantify the Flow Characteristics Over the Dimpled Surface. As described above, a high-resolution PIV system was used in the present study to conduct detailed flow field measurements to quantify the characteristics of the turbulent boundary layer flow over the dimpled test plate in comparison with those over the flat plate. The PIV measurements were conducted in the vertical plane passing the center of the dimple in the middle of the dimpled test plate, i.e., in the *X–Y* plane shown in Fig. 2. Figure 7 shows the typical PIV measurement results over the dimpled surface in the terms of instantaneous velocity field, the instantaneous vorticity distribution, the ensemble-averaged flow velocity field, and "in-plane" TKE of $0.5(\overline{u'^2} + \overline{v'^2})/\bar{U}^2$ for the test case of Re = 50.5 K. The PIV measurement results of the turbulent boundary layer flow over the flat surface were also given in the figure as the comparison baseline. It should be noted that PIV measurements were also conducted for

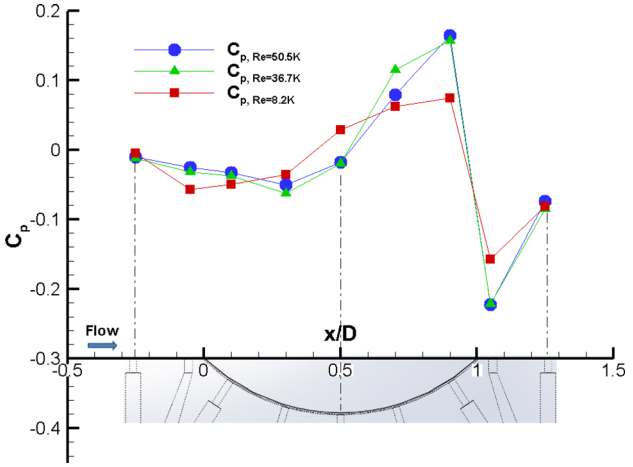

Fig. 6 The profiles of the surface pressure coefficient along the centerline of the dimple

the other test cases with Re = 8.2 K and 36.7 K. Since very similar flow features were seen for the other test cases, only the PIV measurement results for the test case of Re = 50.5 K are shown here for conciseness.

As shown clearly and quantitatively in the instantaneous velocity and vorticity distributions given in Fig. 7, the vortex structures in the boundary layer flow over the dimpled surface were found to become much more complex in compared with those over the flat surface. While only very few vortex structures were identified in the boundary layer flow over the flat test plate, a series of unsteady vortex structures were found to be generated and shed periodically from both the front and back rims of the dimple as the incoming mainstream flow passing over the dimple. After shedding from the front and back rims of the dimple, the unsteady vortex structures were found to break down into smaller vortices as they moving downstream. As a result, the turbulent boundary layer flow over the dimpled surface was found to be filled with various vortex structures with different size and orientations. The instantaneous PIV measurement result also reveals clearly that a strong upwash flow was generated near the back rim of the dimple, which would greatly enhance the turbulent mixing between the low-momentum flow near the wall and the high-momentum freestream flow further away from the wall. As a result, the heat transfer process between the hot flow near the wall and the mainstream coolant flow would be augmented due to the existence of the dimple arrays over the dimpled plate. The upwash flow generated at the back rim of the dimple and the enhanced turbulent mixing in the boundary layer flow over the dimpled surface can also be seen clearly in the ensemble-averaged velocity field and the in-plane TKE distributions given in Fig. 7.

Based on qualitative visualization with smoke wire, Ligrani et al. [3,19] conducted a series of experimental studies to examine the relationship between the enhanced local heat transfer and the characteristics of the flow structures over dimpled surfaces. They suggested that the vortex structures shedding from the dimples (including large upwash regions and packets of vortices generated from the dimples) would enhance the turbulence mixing between the mainstream coolant flow and the hot flow inside the dimples, therefore, leading to an augmentation of local heat transfer near the rims of dimples. The existence of the strong upwash flow and packets of unsteady vortex structures over the dimpled surface revealed quantitatively from the PIV measurements described above was found to be in good agreement with the qualitative smoke wire visualization results reported in Ligrani et al. [3,19]. While TKE level is usually used as an index to evaluate the extent of the fluid mixing in a turbulent flow, as shown quantitatively in the in-plane TKE distributions given in Fig. 7, the appearance of a region with high in-plane TKE levels near the back rim of the

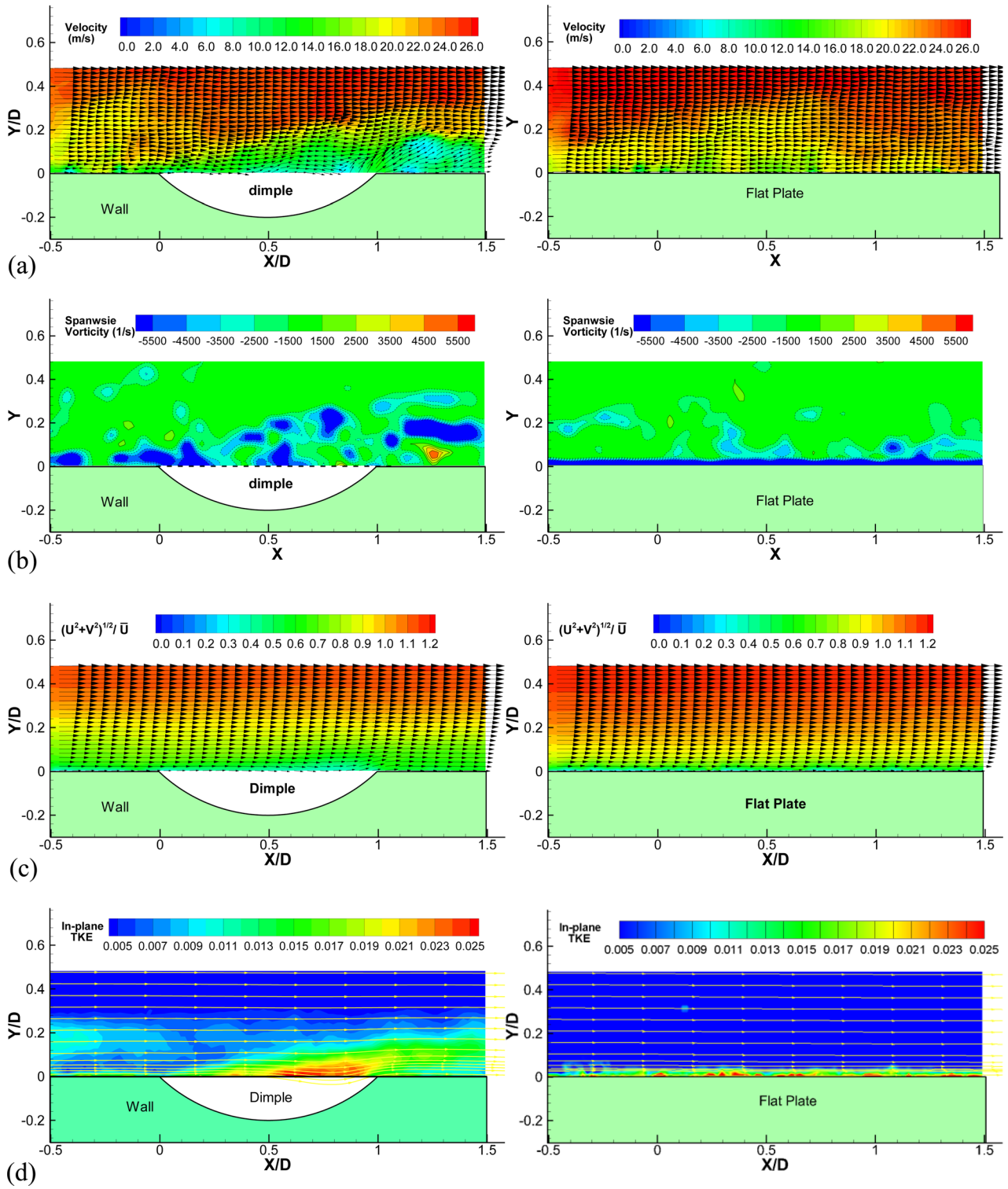

Fig. 7 PIV measurements of the flow field over the dimpled and flat surfaces at Re = 50.5 K: (*a*) Instantaneous velocity field over the dimpled (left) and flat (right) surfaces, (*b*) instantaneous vorticity distributions over the dimpled (left) and flat (right) surfaces, (*c*) mean velocity field over the dimpled (left) and flat (right) surfaces, and (*d*) in-plane TKE distribution over the dimpled (left) and flat (right) surfaces

dimple illustrates a strong correlation between the enhanced turbulent mixing in the boundary layer flow over the dimpled surface with the improved local heat transfer in the region near the back rim of the dimple reported in Ligrani et al. [3,19], which will be addressed in further detail in the later section of the present study.

While the PIV measurement results given in Fig. 7 reveal the significant differences in the characteristics of the turbulent boundary layer flows over the dimpled surface, in comparison with those over a conventional flat surface, it is highly desirable to conduct quantitative measurements to examine the flow features inside the dimple cavity in order to gain a more intuitive insight into the underlying physics. As described above, by tilting the camera for PIV image acquisition with an angle of 30 deg to the vertically aligned laser sheet along the middle plane of the

dimpled test plate (i.e., X–Y plane as shown in Fig. 2), the flow field inside the dimple was also measured in the present study by using the high-resolution PIV system. Figures 8–10 give the typical PIV measurement results to reveal the flow characteristics inside the dimple cavity for the test cases with Re = 8.2 K, 36.7 K, and 50.5 K, respectively.

As revealed clearly in the PIV measurement results, the flow features inside the dimple cavity were found to be actually quite complicated. While the flow velocity inside the dimple was found to be relatively small in general as expected, a large recirculating flow was found to form inside the dimple. The high-speed incoming mainstream flow was found to separate from the wall surface when passing over the front rim of the dimple. Due to the Kelvin–Helmholtz instabilities [32] in the shear layer between the high-speed mainstream flow and the low-speed recirculating flow inside the dimple cavity, unsteady vortex structures were found to be generated and shed periodically along the interface between the two flow streams. It should be noted that Tollmien–Schlichting (T–S) instability may also contribute to the generation of unsteady vortices structures in the boundary layer flow over the dimpled surface.

The generation and periodic shedding of the unsteady Kelvin–Helmholtz vortices would cause intensive turbulent mixing in the boundary layer flow over the dimple not only by promoting the entrainment of high-speed mainstream flow from outside into the near-wall region, but also boosting the ejection of the low-speed recirculating flow out of the dimple cavity. As a result, the heat transfer process between the high-speed coolant flow and the near-wall hot flow over the dimpled surface is greatly enhanced, as reported in Ligrani et al. [3,19].

The PIV measurement results also reveal clearly that, due to the existence of the low pressure at the front of the dimple cavity as shown clearly in Fig. 5, the high-speed mainstream flow would shift downward slightly and impinge onto the back rim of the dimple, creating a strong upwash flow near the back rim of the dimple. As described above, the impingement of the high-speed mainstream flow onto the back rim of the dimple would result in a high pressure region over the back portion of the dimple cavity,

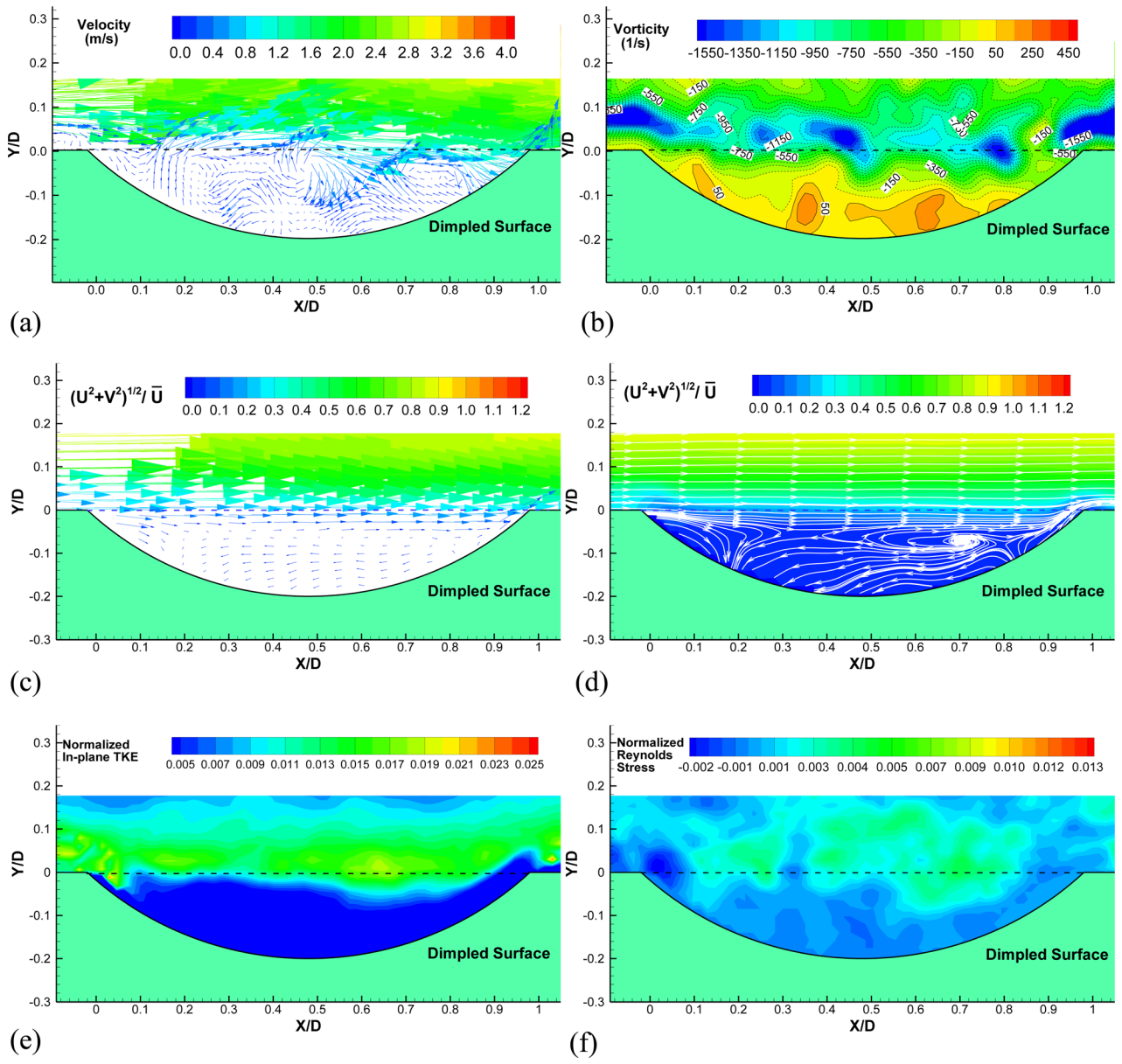

Fig. 8 PIV measurement results of the flow field inside the dimple at Re = 8.2 K: (*a*) instantaneous velocity field, (*b*) instantaneous vorticity distribution, (*c*) ensembles-averaged velocity field, (*d*) streamlines of the mean flow field, (*e*) normalized in-plane TKE distribution, and (*f*) normalized Reynolds stress distribution

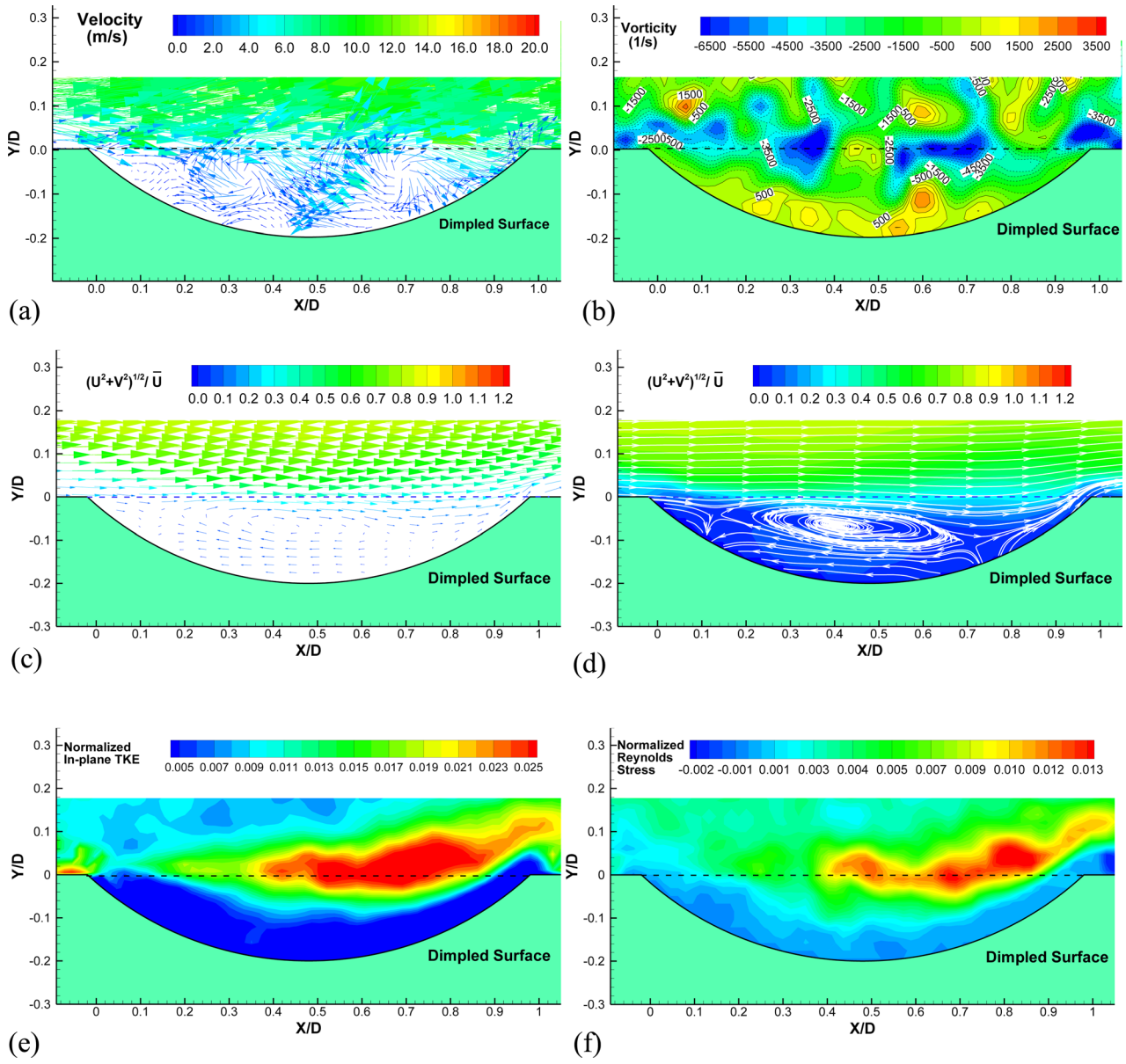

Fig. 9 PIV measurement results of the flow field inside the dimple at Re = 36.7 K: (*a*) instantaneous velocity field, (*b*) instantaneous vorticity distribution, (*c*) ensembles-averaged velocity field, (*d*) streamlines of the mean flow field, (*e*) normalized in-plane TKE distribution, and (*f*) normalized Reynolds stress distribution

which is also revealed clearly and quantitatively from the surface pressure distributions given in Fig. 5. As shown clearly in the normalized in-plane TKE and Reynolds stress distributions given in Figs. 8–10, the regions with high TKE and Reynolds stress values were found to concentrate mainly in the shear layer between the high-speed mainstream flow and the low-speed recirculating flow inside the dimple cavity, which is correlated well with the shedding path of the unsteady Kelvin–Helmholtz vortices described above. Corresponding to the formation of the strong upwash flow near the back rim of the dimple, the TKE and Reynolds stress values were found to increase significantly in region near the back rim of the dimple.

While the global features of the flow characteristics inside the dimple were found to be quite similar in general for the test cases with different Reynolds number levels, some differences still can be identified by carefully inspecting the PIV measurement results for the three compared cases. As shown in the ensemble-averaged velocity fields and the corresponding streamline distributions, while the center of the recirculation zone inside the dimple cavity was found to move further forward to the front rim of the dimple, the recirculating flow inside the dimple would much become stronger, as the Reynolds number increases. This explains the larger size of the region with relative low surface pressure at the front portion of the dimple for the cases with higher Reynolds numbers, as shown in Fig. 5. It can also be seen that the upwash flow near the back rim of the dimple would become much stronger as the Reynold number increases, which results in higher normalized in-plane TKE and Reynolds stress levels in the boundary layer flow over the dimpled surface.

Figure 11 shows a schematic sketch of the flow features over a dimple, which vividly illustrates the unique flow characteristics and evaluation of the unsteady vortex structures revealed from the measured surface pressure distributions and PIV measurement results given above. As shown in the diagram, the incoming high-speed mainstream flow would separate from the dimpled surface when passing over the front rim of the dimple, which leads to the formation of a strong shear layer between the high-speed mainstream flow and the low-speed recirculating flow inside the dimple

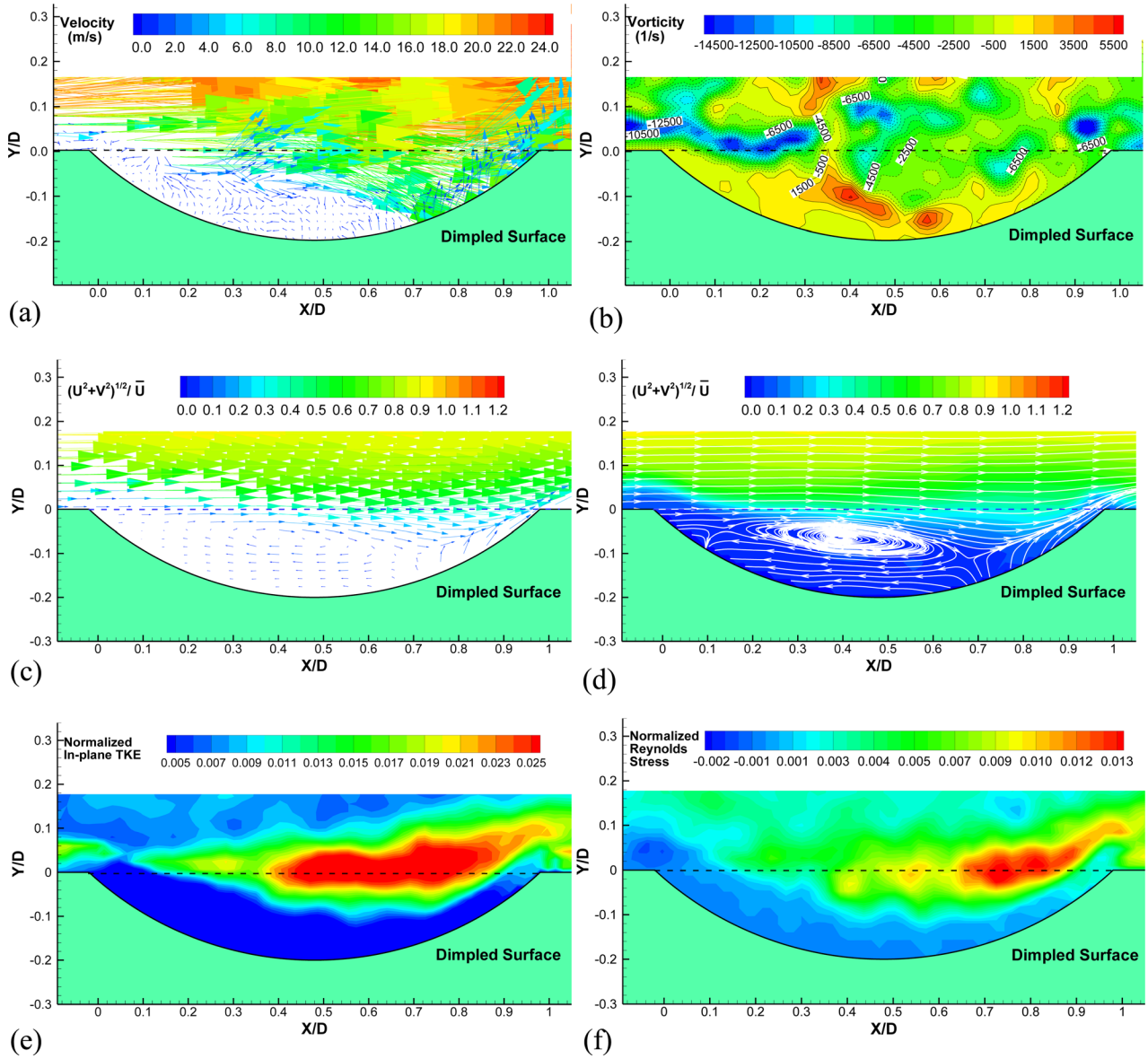

Fig. 10 PIV measurement results of the flow field inside the dimple at Re = 50.5 K: (*a*) instantaneous velocity field, (*b*) instantaneous vorticity distribution, (*c*) ensembles-averaged velocity field, (*d*) streamlines of the mean flow field, (*e*) normalized in-plane TKE distribution, and (*f*) normalized Reynolds stress distribution

cavity. The separated boundary layer flow over the dimple would behave more like a free shear layer which is highly unstable; therefore, rolling up of unsteady vortex structures due to the Kelvin–Helmholtz instabilities would be readily realized. As shown schematically in Fig. 11, the unsteady Kelvin–Helmholtz vortices will not only promote the entrainment of high-speed mainstream flow from outside into the near-wall region but also booster the ejection of the low-speed recirculating flow out of the

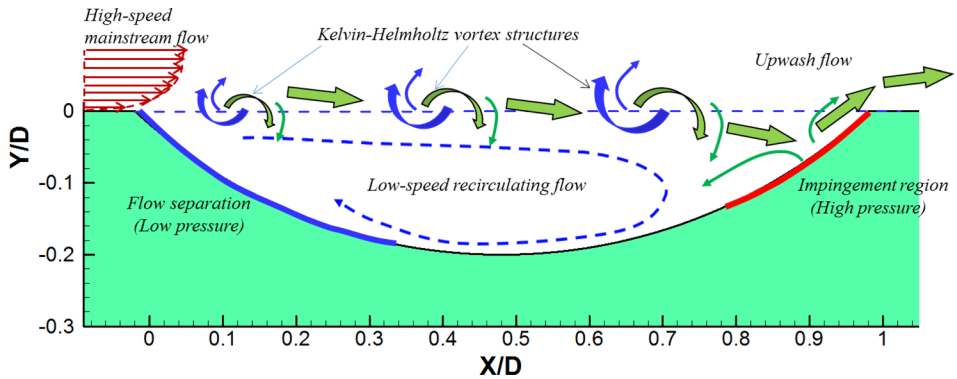

Fig. 11 Schematic of the flow structures inside a dimple cavity

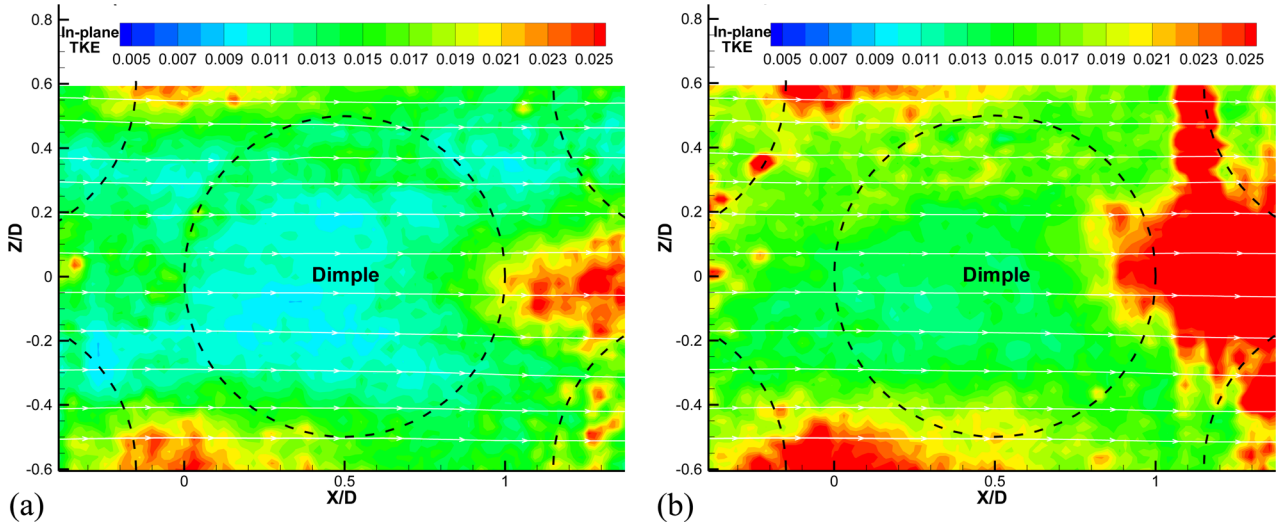

Fig. 12 Distributions of the normalized in-plane TKE (i.e., $0.5(\overline{u'^2}+\overline{w'^2})/\bar{U}^2$) in the horizontal plane near the upper surface of the dimpled test plate: (*a*) Re = 36.7 K and (*b*) Re = 50.5 K

dimple cavity. The ejection of the low-speed recirculating flow inside the dimple cavity into the high-speed mainstream flow will result in the formation of so-called "mushroom vortex" structures as described in Mahmood et al. [7]. The existence of the low pressure region at the front portion of the dimple, which is correlated to the formation of the low-speed recirculating flow inside the dimple cavity, will cause the high-speed mainstream flow to shift downward slightly and impinge onto the back rim of the dimple. After the impingement, the flow would split into two streams with one stream recirculating inside the dimple cavity and the other ejected out of the dimple cavity as a strong upwash flow. With such a process, the dimple acts as a "turbulator" to generate various unsteady vortex structures and strong upwash flow in the boundary layer flow over the dimpled surface to promote the turbulent mixing between the high-speed coolant flow and the hot low-speed flow inside the dimple cavity. This is believed to be the primary reason why a dimpled surface can have a good heat transfer enhancement performance with comparatively smaller pressure loss penalties, in comparison to other types of heat transfer augmentation devices such as pin-fins and rib turbulators used for the internal cooling of turbine blades.

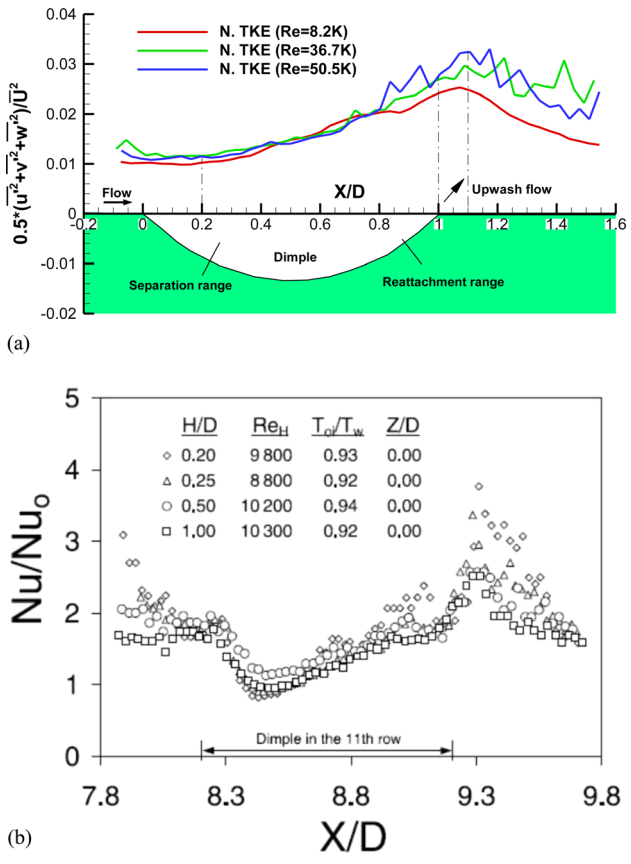

Fig. 13 (*a*) Measured TKE profiles of the present study and (*b*) Measured local Nusselt number data reported in Mahmood and Ligrani [15]

It should also be noted that while Mahmood et al. [7,15] and Ligrani et al. [3,19] conducted a series of experimentally studies to investigate the unsteady vortex and turbulent flow structures on and above dimple arrays as well as their correlations to the enhanced heat transfer performance of dimpled surfaces, most of the research findings were derived based on qualitative flow visualization images obtained with a smoke wire method to visualize flow features on and above dimpled surfaces, very limited quantitative information about the flow characteristics and unsteady vortex structures has ever been reported in previous studies. The quantitative measurement results given in the present study are believed to be the first of its nature to quantify the unique flow characteristics and evolution of the unsteady vortex structures inside the dimple cavity and the enhanced turbulent mixing in the boundary layer flow over the dimpled surface. The formation and shedding of the unsteady Kelvin–Helmholtz vortices, the impingement of the high-speed mainstream flow onto the dimple back rim, and the subsequent generation of strong upwash flow to promote the turbulent mixing over the dimpled surface were revealed clearly and quantitatively from the PIV measurement results given above. In comparison with the qualitative flow visualization images reported in Mahmood et al. [7,15] and Ligrani et al. [3,19], the quantitative flow field measurement results given in the present study depict a much more vivid picture about the unique flow characteristics and evolution of the unsteady vortex structures on and above dimpled surface, which is highly desirable to elucidate underlying physics to gain further insight into underlying physics and to explore/optimize design paradigms for better internal cooling designs to protect turbine blades from the extremely harsh environments.

In the present study, PIV measurements were also conducted in a horizontal plane parallel to the dimpled test plate, i.e., in the *X*–*Z* plane as shown in Fig. 2. For the PIV measurements in the horizontal plane, the laser sheet was set to be about 1.5 mm away

from the upper surface of the dimpled test plate (i.e., $Y/D \approx 0.08$) in order to minimize the strong reflection of the illuminating laser sheet from the upper surface of the test plate. Figure 12 shows typical PIV measurement results in the terms of the normalized in-plane TKE distribution (i.e., $0.5(\overline{u'^2} + \overline{w'^2})/\bar{U}^2$) for the test cases of Re = 36.7 K and 50.5 K. Corresponding to the generation of upwash flows near the back rims of the dimples as shown schematically in Fig. 11, regions with high TKE values can be seen clearly near the back rims of the dimples. It can also be seen that while the magnitudes of the normalized in-plane TKE values in the boundary layer flow over the dimpled surface were found to become greater as the Reynolds number increases, the regions with relatively greater TKE values near the back rims of the dimples were also found to become much wider for the case with higher Reynolds numbers.

It is well known that convective heat transfer process over a heated surface is closely related to the flow characteristics of the turbulent boundary layer over the surface. TKE is one of the most widely used quantities to indicate the extent of turbulent mixing in a turbulent flow. A much higher TKE level would indicate more intensive mixing in the turbulent flow, which would lead to a stronger convective heat transfer process. With an infrared thermography technique to quantify local heat transfer characteristics of dimpled arrays at different Reynolds numbers, Mahmood and Ligrani [15] found that the regions with high local Nusselt number levels are usually located near the back rims of dimples, which is correlated very well with the regions with high TKE levels, as shown in Fig. 12.

In the present study, by combining the two-dimensional PIV measurement results of the *in-plane* TKE in the vertical plane (i.e., $0.5(\overline{u'^2} + \overline{v'^2})/\bar{U}^2$ as shown in Figs. 8–10) and the horizontal plane (i.e., $0.5(\overline{u'^2} + \overline{w'^2})/\bar{U}^2$ as shown in Fig. 12), the normalized TKE (i.e., TKE $= 0.5(\overline{u'^2} + \overline{v'^2} + \overline{w'^2})/\bar{U}^2$) of the boundary layer flow over the dimpled surface can be determined. Figure 13(*a*) shows the profiles of the normalized TKE along the centerline of the dimple in the $Y/D \approx 0.08$ plane. The heat transfer measurement results of Mahmood and Ligrani [15] in the term of measured local Nusselt number along the centerline of a dimple at similar test conditions as those used in the present study were given in Fig. 13(*b*) for qualitative comparison. As shown clearly in Fig. 13(*a*), the normalized TKE levels were found to decrease slightly in the region over the front portion of the dimple, and reaching their minimum values at the downstream location of $X/D \approx 0.2$. The normalized TKE values were found to increase gradually afterward as the downstream distance increases, reaching their maximum peaks at the downstream location of $X/D \approx 1.1$, and then decrease gradually at further downstream locations. The general trend of the normalized TKE profiles of the present study was found to match well with that revealed from the measured local Nusselt number profiles of Mahmood and Ligrani [15] given in Fig. 13(*b*). As shown in schematically in Fig. 11, since the low-speed recirculating flow inside the dimple cavity would trap the hot fluid inside the dimple cavity, the heat transfer process over the wall surface near the front rim of the dimple would be deteriorated. As a result, the local Nusselt number was found to decrease gradually over the wall surface near the front rim of the dimple, as shown clearly in Fig. 13(*b*). Due to the impingement of the high-speed coolant flow onto the wall surface near the back rim of the dimple, a strong upwash stream is generated in the boundary layer flow over the back portion of the dimple, which would significantly enhance the turbulent mixing in the boundary layer flow over the back portion of the dimpled surface, consequently, augment the heat transfer process between the high-speed coolant flow and the low-speed hot flow over the wall surface near the back rim of the dimple. Therefore, the local Nusselt number was found to increase continuously over the surface at the back portion of the dimple. As described in Mahmood and Ligrani [15], the measured local Nusselt number would reach their minimum and maximum values at about $0.2D$ and $1.1D$ away from of the front rim of the dimple, which are found to correlate very well with the positions of the minimum and maximum peaks of the normalized TKE (i.e., at the downstream locations of $X/D \approx 0.2$ and $X/D \approx 1.1$) revealed in the normalized TKE profiles shown in Fig. 13(*a*).

4 Conclusions

In the present study, an experimental investigation was conducted to quantify the characteristics of the boundary layer flow on and over a dimpled surface in comparison to those over a conventional flat plate. The experimental study was conducted in a low-speed, open-circuit wind tunnel with the Reynolds number (i.e., based on the hydraulic diameter of the dimpled channel and freestream velocity) of the test cases in the range of Re = 8200–50,500. In addition to measuring surface pressure distributions to determine the friction factors of the test plates and to reveal detailed surface pressure map inside a dimple cavity, a high-resolution digital PIV system was used to achieve detailed flow field measurements to quantify the characteristics of the turbulent boundary layer flows over the dimpled test plate and the evolution of the unsteady vortex structures inside the dimple cavity at the middle of the dimpled test plate.

It was found that the friction factor of the dimpled test plate would be about 30–80% higher than that of the conventional flat plate, depending on the Reynolds number of the test cases, which agrees well with the findings reported in previous studies. The detailed surface pressure measurements inside the dimple cavity at the middle of the dimpled test plate reveal clearly that, while the surface pressure in the front portion of the dimple was found to be relatively low, a region with much high surface pressure would exist near the back rim of the dimple. Such a surface pressure distribution pattern was found to be closely related to the unique flow characteristics inside the dimple cavity.

As shown clearly and quantitatively from the PIV measurement results, the high-speed incoming mainstream flow would separate from the dimpled surface when passing over the front rims of the dimples. The separated boundary layer flow was found to behave more like a free shear layer which is highly unstable; therefore, rolling up of unsteady vortex structures due to the Kelvin–Helmholtz instabilities in the shear layer between the high-speed mainstream flow and the low-speed recirculating flow inside the dimple cavity would be readily realized. The unsteady Kelvin–Helmholtz vortices were found to be able to not only promote the entrainment of high-speed mainstream flow into the near wall region, but also booster the ejection of the low-speed recirculating flow out of the dimple cavity. The existence of the low pressure region at the front portion of the dimple, which is correlated to the formation of the low-speed recirculation zone inside the dimple cavity, would cause the high-speed mainstream flow to shift downward slightly and impinge onto the back rim of the dimple. Consequently, a strong upwash stream was generated, which would significantly enhance the turbulent mixing in the boundary layer flow over the back portion of the dimpled surface. With such a process, a dimple would act as a "turbulator" to generate unsteady vortex structures and a strong upwash to promote the turbulent mixing in the boundary layer flow over the dimpled surface, thereby, to enhance the heat transfer between the high-speed mainstream flow (i.e., coolant stream) and the low-speed near-wall flow (i.e., hot flow) over the dimpled surface. This is believed to be the primary reason why a dimpled surface can have a good heat transfer enhancement performance with comparatively smaller pressure loss penalties, in comparison to other types of heat transfer augmentation devices such as pin-fins and rib turbulators used for the internal cooling of turbine blades.

The quantitative measurement results given in the present study are believed to be the first of its nature to quantify the characteristics of the boundary layer flows over dimpled surfaces and evolution of the unsteady vortex structures inside dimple cavities, which depict a vivid picture about the unique flow features on and above a dimpled surface and their correlations with the enhanced heat transfer performance. Such quantitative information is highly

desirable to elucidate underlying physics to gain further insight into underlying physics and to explore/optimize design paradigms for better internal cooling designs to protect turbine blades from the extremely harsh environments.

Acknowledgment

The technical assistances of Mr. Bill Richard and Mr. Kai Zhang of Iowa State University are greatly appreciated. Support from the National Science Foundation with Grant Nos. IIA-1064235 and CBET-1064196, is gratefully acknowledged. Y. Rao also wants to thank the support from the National Natural Science Foundation of China (No. 51176111).

References

[1] Han, J., Dutta, S., and Ekkad, S., 2012, *Gas Turbine Heat Transfer and Cooling Technology*, Taylor and Francis, New York.
[2] Han, J., and Wright, L., 2006, "Enhanced Internal Cooling of Turbine Blades and Vanes," *The Gas Turbine Handbook*, DoE-National Energy Technology Laboratory (NETL), http://204.154.137.14/technologies/coalpower/turbines/refshelf.html
[3] Ligrani, P. M., Harrison, J. L., Mahmmod, G. I., and Hill, M. L., 2001, "Flow Structure Due to Dimple Depressions on a Channel Surface," Phys. Fluids, **13**(11), pp. 3442–3451.
[4] Xie, G., Liu, J., Ligrani, P. M., and Zhang, W., 2013, "Numerical Predictions of Heat Transfer and Flow Structure in a Square Cross-Section Channel With Various Non-Spherical Indentation Dimples," Numer. Heat Transfer, Part A, **64**(3), pp. 187–215.
[5] Mitsudharmadi, H., Tay, C., and Tsai, H., 2009, "Effect of Rounded Edged Dimple Arrays on the Boundary Layer Development," J. Vis., **12**(1), pp. 17–25.
[6] Neil Jordan, C., and Wright, L. M., 2012, "Heat Transfer Enhancement in a Rectangular (AR = 3:1) Channel With V-Shaped Dimples," ASME J. Turbomach., **135**(1), p. 011028.
[7] Mahmood, G., Hill, M., Nelson, D., and Ligrani, P., 2001, "Local Heat Transfer and Flow Structure on and Above a Dimpled Surface in a Channel," ASME J. Turbomach., **123**(1), pp. 115–123.
[8] Chyu, M. K., and Siw, S. C., 2013, "Recent Advances of Internal Cooling Techniques for Gas Turbine Airfoils," ASME J. Therm. Sci. Eng. Appl., **5**(2), p. 021008.
[9] Rao, Y., Feng, Y., Li, B., and Weigand, B., 2014, "Experimental and Numerical Study of Heat Transfer and Flow Friction in Channels With Dimples of Different Shapes," ASME J. Heat Transfer, **137**(3), p. 031901.
[10] Rao, Y., Xu, Y., and Wan, C., 2012, "A Numerical Study of the Flow and Heat Transfer in the Pin Fin-Dimple Channels With Various Dimple Depths," ASME J. Heat Transfer, **134**(7), p. 071902.
[11] Chyu, M., Yu, Y., and Ding, H., 1999, "Heat Transfer Enhancement in Rectangular Channels with Concavities," J. Enhanced Heat Transfer, **6**(6), pp. 429–439.
[12] Terekhov, V., Kalinina, S., and Mshvidobadze, Y., 1997, "Heat Transfer Coefficient and Aerodynamic Resistance on a Surface With a Single Dimple," J. Enhanced Heat Transfer, **4**(2), pp. 131–145.
[13] Moon, H. K., O'Connell, T., and Glezer, B., 2000, "Channel Height Effect on Heat Transfer and Friction in a Dimpled Passage," ASME J. Eng. Gas Turbines Power, **122**(2), pp. 307–313.
[14] Ligrani, P., 2013, "Heat Transfer Augmentation Technologies for Internal Cooling of Turbine Components of Gas Turbine Engines," Int. J. Rotating Mach., **2013**, p. 275653.
[15] Mahmood, G., and Ligrani, P., 2002, "Heat Transfer in a Dimpled Channel: Combined Influences of Aspect Ratio, Temperature Ratio, Reynolds Number, and Flow Structure," Int. J. Heat Mass Transfer, **45**(10), pp. 2011–2020.
[16] Turnow, J., Kornev, N., Zhdanov, V., and Hassel, E., 2012, "Flow Structures and Heat Transfer on Dimples in a Staggered Arrangement," Int. J. Heat Fluid Flow, **35**, pp. 168–175.
[17] Bunker, R., and Donnellan, K., 2003, "Heat Transfer and Friction Factors for Flows Inside Circular Tubes With Concavity Surfaces," ASME Paper No. GT2003-38053.
[18] Choi, E., Choi, Y., and Lee, W., 2013, "Heat Transfer Augmentation Using a Rib–Dimple Compound Cooling Technique," Appl. Therm. Eng., **51**(1), pp. 435–441.
[19] Ligrani, P. M., Oliveira, M. M., and Blaskovich, T., 2012, "Comparison of Heat Transfer Augmentation Techniques," AIAA J., **41**(3), pp. 337–362.
[20] Viswanathan, A. K., and Tafti, D. K., 2006, "A Comparative Study of DES and URANS for Flow Prediction in a Two-Pass Internal Cooling Duct," ASME J. Fluids Eng., **128**(6), pp. 1336–1345.
[21] Joo, J., and Durbin, P., 2009, "Simulation of Turbine Blade Trailing Edge Cooling," ASME J. Fluids Eng., **131**(2), p. 021102.
[22] Bogard, D. G., 2006, "Airfoil Film Cooling," *The Gas Turbine Handbook*, National Energy Technology Laboratory, DoE-National Energy Technology Laboratory (NETL), Sec. 4.2.2.1, http://204.154.137.14/technologies/coalpower/turbines/refshelf.html
[23] Ling, J., Rossi, R., and Eaton, J. K., 2014, "Near Wall Modeling for Trailing Edge Slot Film Cooling," ASME J. Fluids Eng., **137**(2), p. 021103.
[24] Farhadi-Azar, R., Ramezanizadeh, M., Taeibi-Rahni, M., and Salimi, M., 2011, "Compound Triple Jets Film Cooling Improvements Via Velocity and Density Ratios: Large Eddy Simulation," ASME J. Fluids Eng., **133**(3), p. 031202.
[25] Soloff, S. M., Adrian, R. J., and Liu, Z.-C., 1997, "Distortion Compensation for Generalized Stereoscopic Particle Image Velocimetry," Meas. Sci. Technol., **8**(12), pp. 1441–1454.
[26] Schlichting, H., and Gersten, K., 2000, *Boundary-Layer Theory*, Springer Science & Business Media, New York.
[27] Pope, S., 2000, *Turbulent Flows*, Cambridge University Press, Cambridge, UK.
[28] Munson, B., Rothmayer, A., and Okiishi, T., 2012, *Fundamentals of Fluid Mechanics*, 6th ed., Wiley Global Education, Hoboken, NJ.
[29] Liu, T., Makhmalbaf, M. H. M., Vewen Ramasamy, R., Kode, S., and Merati, P., 2015, "Skin Friction Fields and Surface Dye Patterns on Delta Wings in Water Flows," ASME J. Fluids Eng., **137**(7), p. 071202.
[30] He, S., and Gotts, J. A., 2004, "Calculation of Friction Coefficients for Noncircular Channels," ASME J. Fluids Eng., **126**(6), pp. 1033–1038.
[31] Dean, R. B., 1978, "Reynolds Number Dependence of Skin Friction and Other Bulk Flow Variables in Two-Dimensional Rectangular Duct Flow," ASME J. Fluids Eng., **100**(2), pp. 215–223.
[32] Yang, L., Ligrani, P., Ren, J., and Jiang, H., 2015, "Unsteady Structure and Development of a Row of Impingement Jets, Including Kelvin–Helmholtz Vortex Development," ASME J. Fluids Eng., **137**(5), p. 051201.